Rapid solidification behavior of Cu–Co–Fe alloy

Lei Zhao and Jiu Zhou Zhao[a)]
Institute of Metal Research, Chinese Academy of Sciences, Shenyang, Liaoning 110016, People's Republic of China

(Received 9 November 2012; accepted 18 March 2013)

The ternary Cu–Co–Fe alloy was rapidly solidified by using the high pressure gas atomization technique. Powders with a well-dispersed microstructure resulting from the liquid–liquid phase transformation were obtained. A model describing the microstructure evolution in an atomized drop during the liquid–liquid phase transformation was developed. The kinetic details of the liquid–liquid phase transformation were discussed. The numerical results show a favorable agreement with the experimental ones. They demonstrate that under the rapid cooling conditions of gas atomization, the spatial phase separation due to the Marangoni migration of the minority phase droplets is very weak. Also, the effect of Ostwald coarsening of the minority phase droplets on the microstructure is negligible. For Cu-10 wt% Co-10 wt% Fe alloy, the average radius and number density of the Fe–Co-rich particles depend exponentially on the cooling rate of the melt during the nucleation period of the Fe–Co-rich droplets.

I. INTRODUCTION

Cu–Co and Cu–Fe alloys, whose phase diagrams show a metastable miscibility gap in the liquid state, are good candidates to be used as the advanced electrical and magnetic materials.[1,2] For example, they are especially suitable for the applications in the manufacturing of electric contactor, semiconductor lead frames, wires and cables, magnetic recording, and magnetic sensors. These alloys, however, have an essential drawback that the miscibility gap poses problems during solidification. When such an alloy is cooled into the miscibility gap, it develops into two liquids.[3,4] Generally, the liquid–liquid phase transformation leads to a microstructure with a serious phase segregation under the conventional solidification conditions. Research indicates that rapid solidification techniques may have great potentials in the manufacturing of this kind of alloys.[5,6]

In recent years, Cu–Co–Fe system was used as a model alloy for the experimental and theoretical studies of the solidification behaviors of the alloys with a metastable miscibility gap in the liquid state.[7] Many researchers[8–10] measured experimentally the liquidus temperature and the liquid–liquid phase transformation temperature (binodal line temperature) of this system. Thermodynamic optimizations have been done by Turchanin et al.,[7] Bamberger et al.,[11] Wang et al.,[12] and Palumbo et al.[13] to establish the phase diagram of Cu–Co–Fe. Experiments have been carried out to investigate the solidification behaviors of Cu–Co–Fe alloy.[9,14] However, the microstructure evolution of this alloy remains unclear up to date because the kinetic process of the liquid–liquid phase transformation is very complex.

We carried out rapid solidification experiment with Cu–Co–Fe alloy by using the high-pressure gas atomization technique. A model describing the microstructure formation in an atomized drop of Cu–Co–Fe during the liquid–liquid phase transformation alloy was developed. The model was first verified by comparing with the experimental results and then applied to investigate the kinetic details of the microstructure formation in the gas atomized drops of Cu–Co–Fe alloy.

II. EXPERIMENTAL PROCEDURES AND RESULTS

Cu-10 wt% Co-10 wt% Fe alloy was prepared by using Cu, Co, and Fe with a purity of 99.9% or higher. Figure 1 shows the schematic diagram of the atomized apparatus. The experimental procedures are as follows. Firstly, the raw materials were melted and overheated to 1693 K in a crucible using a vacuum induction furnace. The alloy was held at this temperature for 15–20 min to form a homogeneous, single-phase melt. Secondly, the melt was atomized by high pressure (3 mPa) N_2 gas when it flowed through a thin bore in the bottom of the crucible. The atomized drops solidified while falling in the chamber. Finally, the powders were separated into classes by mechanical sieving and metallographically prepared. The microstructure was examined by using the optical microscopy and scanning electron microscopy.

Figure 2 shows the typical microstructures of the powder of different diameters. An atomized powder of

[a)]Address all correspondence to this author.
e-mail: jzzhao@imr.ac.cn
DOI: 10.1557/jmr.2013.75

 © Materials Research Society 2013

https://doi.org/10.1557/jmr.2013.75 Published online by Cambridge University Press

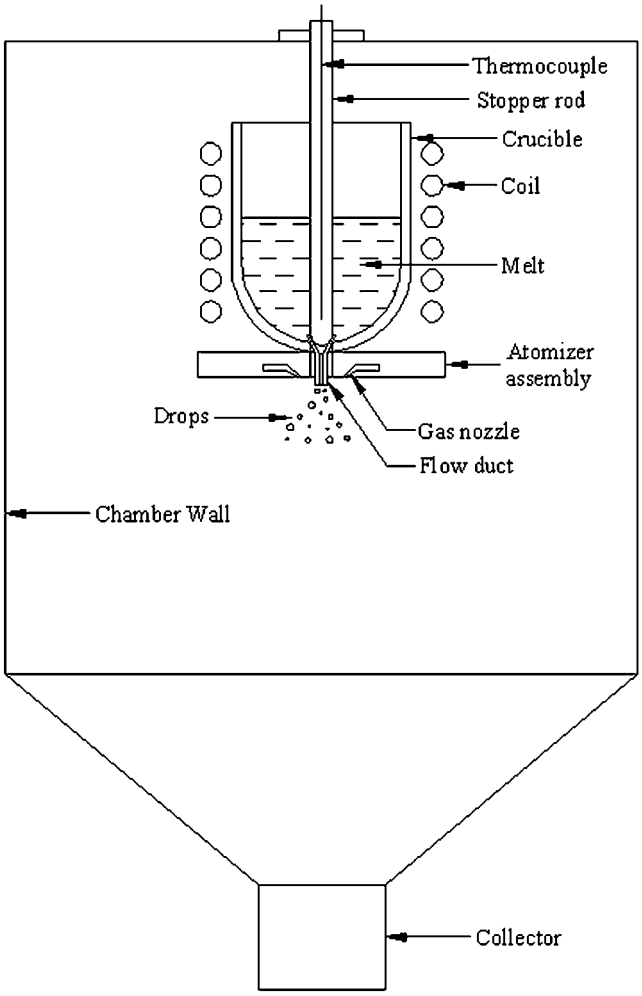


FIG. 1. Schematic diagram of the atomized apparatus.

the diameter <220 μm shows a microstructure consisting of the well-dispersed spherical Fe–Co-rich particles and the Cu-rich matrix. The distributions of the apparent [two-dimensional (2D)] diameter of the Fe–Co-rich particles measured in the section plane of the powders is shown in Fig. 3. The 2D average radius of the Fe–Co-rich particles increases with the powder diameter, as shown in Fig. 4. An atomized powder of the diameter in the range from 280 to 355 μm shows a microstructure consisting of the γ(Fe, Co) dendrites, the spherical Fe–Co-rich particles and the Cu-rich matrix.

III. DISCUSSIONS

A. Rapid solidification process of Cu-10 wt% Co-10 wt% Fe alloy

Figure 5 shows the vertical section x_{Fe}:x_{Co} = 1:1 of the Cu–Co–Fe phase diagram.[8] It indicates that γ(Fe, Co) tends to form in the melt first when a Cu-10 wt% Co-10 wt% Fe alloy is cooled below the liquidus. The liquid–liquid phase transformation may occur only when the melt is cooled into the metastable miscibility gap or achieves an undercooling >24 K.[8] The liquid–liquid phase transformation begins with the nucleation of the liquid Fe–Co-rich droplets. The compositions of the Cu-rich (L_1) and Fe–Co-rich (L_2) liquid phases vary according to the binodal surface in the Cu–Fe–Co phase diagram during the liquid–liquid decomposition as shown in Fig. 5. The Fe–Co-rich droplets tend to solidify (liquid-to-solid phase transformation) during cooling through the metastable miscibility gap under the effect of the undercooling ΔT_{L_2} (see Fig. 5). The transient nucleation rate for the solidification of the Fe–Co-rich droplets may be given by $I_t = I_s \exp(-t/\tau)$ with I_s being the steady-state nucleation rate and τ the incubation time for the nucleation. If the cooling rate of the atomized drop is so fast that the solidification of the Fe–Co-rich droplets does not occur during cooling through the metastable miscibility gap, as for the atomized drops of the diameter <220 μm, the Fe–Co-rich droplets will solidify under the peritectic temperature and the powder shows a microstructure consisting of the matrix phase and the dispersed Fe–Co-rich particles, as shown in Figs. 2(a) and 2(b). Otherwise, the Fe–Co-rich droplets solidify during cooling through the metastable miscibility gap. Because the composition of these particles is close to the composition of the γ(Fe, Co) phase, they may grow directly into the matrix liquid or act as heterogeneous nucleation sets of γ(Fe, Co) phase and cause the formation of the dendritic γ(Fe, Co) phase in the powders as shown in Fig. 2(c).

B. Theoretical model for the microstructure evolution during the liquid–liquid decomposition

When a Cu–Co–Fe alloy is undercooled into the metastable miscibility gap, it transforms into two liquids. The liquid–liquid decomposition begins with the nucleation of the Fe–Co-rich droplets. The nucleation of the Fe–Co-rich droplets can be described with the classical nucleation theory. The stationary homogeneous nucleation rate is given by[15]

$$I = N_0 \cdot O \cdot \Gamma \cdot Z \cdot \exp\left(-\frac{\Delta G_C}{k_B T}\right) \quad , \qquad (1)$$

where $N_0 = (x_A\Omega_A + x_B\Omega_B + x_C\Omega_C)^{-1}$ is the number density of atoms in the liquid. Ω_A, Ω_B, and Ω_C are the atomic volumes of component A, B, and C, respectively. x_A, x_B, and x_C are the mole fractions of component A, B, and C, respectively. $O = 4n_c^{2/3}$ reflects the surface area of the nuclei with n_c being the number of atoms in a droplet of critical radius $R_C = 2\sigma/\Delta G_V$. σ is the interfacial tension between the two liquids. $\Gamma = 6D/\lambda^2$ is the attachment rate of atoms to the droplet with D being the diffusion coefficient and λ the average diffusional jump distance of the atoms.

https://doi.org/10.1557/jmr.2013.75 Published online by Cambridge University Press

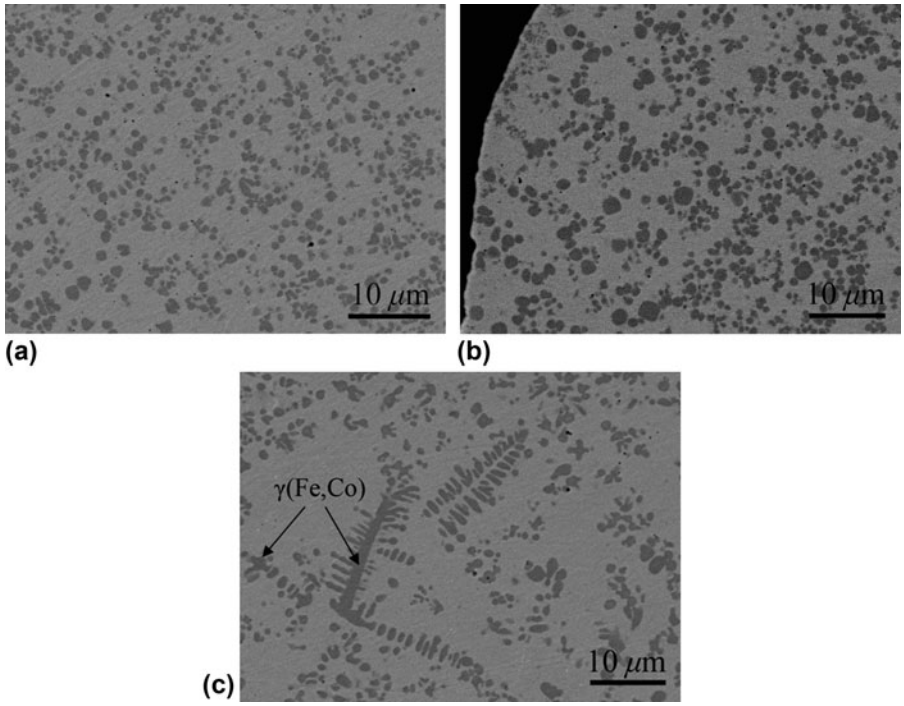


FIG. 2. Microstructure of the Cu-10 wt% Co-10 wt% Fe powders of 125–150 μm (a), 200–220 μm (b) and 280–355 μm (c) in diameter.

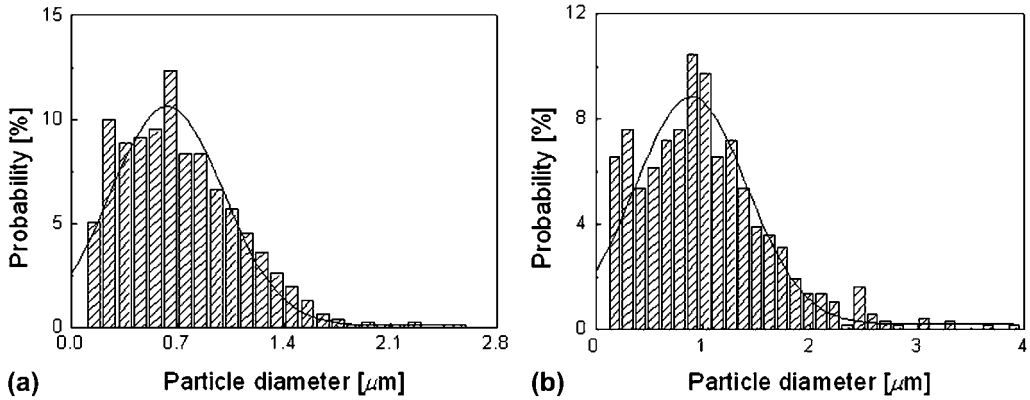


FIG. 3. Size distribution of the Fe–Co-rich particles in the powders of 125–150 μm (a) and 200–220 μm (b) in diameter. The bars are the measured results and the solid curves are the numerical fittings.

$Z = [\Delta G_C/(3\pi k_B T n_c^2)]^{1/2}$ is the Zeldovich factor with k_B being Boltzmann's constant and T the absolute temperature, respectively. $\Delta G_C = 16\pi\sigma^3/(3\Delta G_V^2)$ is the energy barrier for nucleation. $\Delta G_V = \Delta G \cdot V_{mol}^{-1}$ is the gain of the volume free energy on nucleation with V_{mol} being the molar volume of the Fe–Co-rich liquid. ΔG is the molar Gibbs free energy change due to the liquid–liquid phase transformation.

The Fe–Co-rich droplets embedded in a supersaturated matrix grow by diffusional transport of solute in the matrix. Assuming that the composition of the liquid inside a droplet is homogeneous and always follows the phase diagram, the growth rate is given by Eq. (2) if the dimensionless supersaturation $(C_m^i - C_{me}^i)/(C_\beta^i - C_{me}^i)$ is much less than unity.[16,17]

$$V = \frac{dR}{dt} = D^i \frac{C_m^i - C_{mI}^i}{C_\beta^i - C_{mI}^i}\frac{1}{R}\left[1 + R(4\pi N\langle R\rangle)^{1/2}\right] + \frac{R}{3}\frac{\frac{dC_\beta^i}{dT}\frac{dT}{dt}}{C_\beta^i - C_{mI}^i} \quad , \tag{2}$$

where R, $<R>$, and N are the radius, average radius, and number density of the Fe–Co-rich droplets, respectively. C_m^i is the mean field concentration of solute i in the matrix

https://doi.org/10.1557/jmr.2013.75 Published online by Cambridge University Press

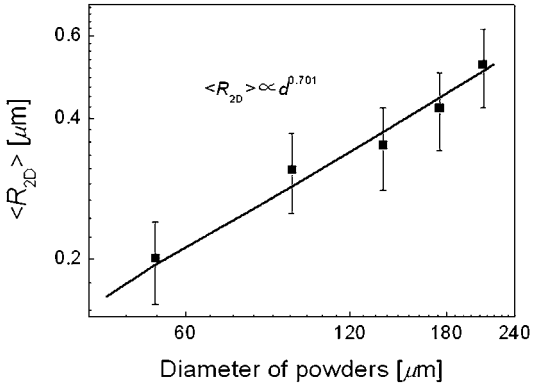


FIG. 4. Experimental results (squares) and numerical results (solid line) of the 2D average radius of the Fe–Co-rich particles ($<R_{2D}>$) as a function of powder diameter (d).

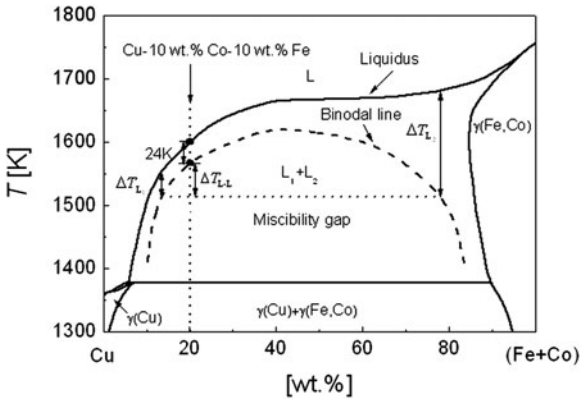


FIG. 5. Vertical section x_{Fe}:x_{Co} = 1:1 (wt%) of the Cu–Co–Fe phase diagram.

liquid. C_{β}^{i} is the concentration of solute i in the Fe–Co-rich droplets. $C_{mI}^{i} = C_{me}^{i}\exp(\alpha_S/R)$ is the concentration of solute i in the matrix at the interphase boundary. $\alpha_S = 2\sigma\Omega^{\beta}/k_B T$ is the capillary length with Ω^{β} being the atomic volume of the Fe–Co-rich droplets and C_{me}^{i} the equilibrium composition of solute i at a flat interface boundary.

To describe the microstructure evolution in an atomized drop during the liquid–liquid phase transformation, a radius distribution function of the Fe–Co-rich droplets $f(R, r, t)$ is defined. $f(R, r, t)\mathrm{d}R$ gives the number of the Fe–Co-rich droplets per unit volume at the position r measured from the center of the atomized drop and at time t in a size class from R to $R + \mathrm{d}R$. Taking into account the concurrent actions of the nucleation, diffusional growth, spatial motion of the Fe–Co-rich droplets due to the Marangoni migration, $f(R, r, t)$ obeys the following continuity equation:

$$\frac{\partial f}{\partial t} + \frac{\partial}{\partial R}(Vf) - \frac{1}{r^2}\frac{\partial(u_m r^2 f)}{\partial r} = \delta_I \quad , \qquad (3)$$

$$u_m = -\frac{2R}{[(2\lambda_m + \lambda_\beta)/\lambda_m](2\eta_m + 3\eta_\beta)}\frac{\partial\sigma}{\partial T}\nabla T \quad , \qquad (4)$$

where u_m is the Marangoni migration velocity of the Fe–Co-rich droplets. λ_m and λ_β are the thermal conductivities of the matrix liquid and the Fe–Co-rich droplets, respectively. η_m and η_β are the dynamic viscosities of the matrix liquid and the Fe–Co-rich droplets, respectively. δ_I is a function related to the nucleation rate of the Fe–Co-rich droplets. $\delta_I(R \neq R_C) = 0$; $\delta_I(R = R_C) = f_I$. f_I is the increasing rate of $f(R_C, r, t)$ due to the nucleation of the Fe–Co-rich droplets. When solving Eq. (3) numerically, f_I is given by $f_I = I/\Delta R$ with ΔR being the step for R. In Eq. (3), the first term describes the time dependence of the distribution function. The second term describes the contribution of the diffusional growth of the Fe–Co-rich droplets to the change of the size distribution function. The third term describes the effect of u_m on the local size distribution function. The last term is the source term due to nucleation. Considering that the collision and coagulation between the Fe–Co-rich droplets show a weak effect on the microstructure formation in an atomized drop,[18] their effects are neglected in Eq. (3).

The temperature field of the atomized drop can be calculated by Eq. (5) using Eq. (6) as the boundary condition.

$$\frac{1}{r^2}\frac{\partial\left(\lambda_H r^2\frac{\partial T}{\partial r}\right)}{\partial r} + Q_{S/L} - \frac{4\pi}{3}\frac{1}{r^2}\frac{\partial\left[r^2\int_0^{\infty} u_m f(R,r,t)(\rho_\beta c_{p\beta} - \rho_m c_{pm})TR^3\,\mathrm{d}R\right]}{\partial r} = \rho c_p\frac{\partial T}{\partial t} \quad , \qquad (5)$$

$$q_d = \pi d^2 h(T_{ds} - T_g) \quad , \qquad (6)$$

where $Q_{S/L} = \rho L_S V_{S/L}$ is the latent heat released at the solidification interface per second, L_S is the latent heat of solidification, $V_{S/L}$ is the moving velocity of the S/L interface. c_p, ρ, and λ_H are, respectively, the specific heat, density, and thermal conductivity of the alloy. ρ_m and c_{pm} are, respectively, the density and specific heat of the matrix liquid. ρ_β and $c_{p\beta}$ are, respectively, the density and specific heat of the Fe–Co-rich droplets. q_d is the heat transfer rate on the surface of the atomized drop.[19] T_{ds} is the surface temperature of the atomized drop. T_g is the temperature of the atomization gas.[20] h is the convective heat-transfer coefficient.[19] In Eq. (5), the first term describes the heat transfer due to conduction, the second term describes the effect of the release of the latent heat due to the solidification, the third term describes the heat transfer due to the motion of the Fe–Co-rich droplets, and the last term

https://doi.org/10.1557/jmr.2013.75 Published online by Cambridge University Press

describes the time dependence of the temperature. Considering that the heat of liquid–liquid phase decomposition is very small in comparison with the solidification latent heat, it is neglected in the calculations.

The solute transfers by both the diffusion of solute in the matrix and the motion of the Fe–Co-rich droplets during cooling an atomized drop. According to the conservation relation of solute, the concentration field of solute i obeys

$$\frac{1}{r^2}\frac{\partial\left(\varphi_l D^i r^2 \frac{\partial S^i}{\partial r}\right)}{\partial r} - \frac{4\pi}{3}\frac{1}{r^2}\frac{\partial\left[r^2\int_0^\infty u_m f(R,r,t)(C^i_\beta - C^i_m)R^3\,dR\right]}{\partial r} = \frac{\partial C^i_{mix}}{\partial t} \quad , \tag{7}$$

where C^i_{mix} is the content of solute i in the local mixture of liquids. $S^i = C^i_m - C^i_{me}$ is the supersaturation of the matrix liquid.[18] φ_l is the volume fraction of the matrix liquid. In Eq. (7), the first and second terms describe the change of solute in the matrix liquid due to the diffusional transfer and the motion of the Fe–Co-rich droplets, respectively. The last term describes the time dependence of the concentration.

Coupling the temperature field and the concentration field given by Eqs. (5) and (7) with the phase diagram of Cu–Co–Fe alloy, the size distribution function of the Fe–Co-rich droplets in the atomized drop is determined via a solution to Eq. (3).

C. Numerical methods

The equations given in the above section are solved numerically by using the finite-volume method. Both the radial axes of the atomized drop and the Fe–Co-rich droplets are divided into a number of intervals, which constitute the finite volumes. The partial differential equations for the temperature field [Eq. (5)] and for the concentration field [Eq. (7)] are, respectively, discredited as the implicit difference equations using the assumption that the temperature and the concentration vary in a stepwise manner in the direction of the atomized drop radial axis (m mesh points). The discretization yields m ordinary differential equations with one equation for each of the m finite volumes for Eq. (5) and also for Eq. (7). Eq. (3) is discredited as an implicit difference equation using the assumption that the radial distribution function varies in a stepwise manner both in the direction of the radial axis of the Fe–Co-rich droplets (n mesh points) and in the direction of the radial axes of the atomized drop. The discretization of the continuous equation yields $m \times n$ ordinary differential equations with one equation for each of the $m \times n$ finite volumes. These equations were solved by using the line-by-line algorithm, which is a combination of the algorithm of Gauss–Seidel and that of Thomas.[21]

The thermodynamic driving force for the liquid–liquid phase transformation and the phase diagram of Cu–Co–Fe alloy were calculated directly from the Gibbs free energy function. The molar Gibbs free energy of mixing of the liquid phase is given by[7]

$$G_m = \sum_{i=Cu,Co,Fe} {}^0G_i x_i + R_g T \sum_{i=Cu,Co,Fe} x_i \ln x_i + {}^E G_m \quad , \tag{8}$$

$$\begin{aligned} {}^E G_m = {} & x_{Cu}x_{Co}L_{Cu,Co} + x_{Cu}x_{Fe}L_{Cu,Fe} + x_{Co}x_{Fe}L_{Co,Fe} \\ & + x_{Cu}x_{Co}x_{Fe}L_{Cu,Co,Fe} \quad , \end{aligned} \tag{9}$$

$$L_{i,j} = \sum_{v=0}^{n} (x_i - x_j)^v \cdot {}^vL_{i,j} \quad , \tag{10}$$

$$L_{i,j,k} = x_i \cdot {}^0L_{i,j,k} + x_j \cdot {}^1L_{i,j,k} + x_k \cdot {}^2L_{i,j,k} \quad , \tag{11}$$

where ${}^0G_i$ and x_i are the Gibbs free energy and the mole fraction of pure component i (i = Cu, Co, Fe), respectively. The Gibbs free energies of the pure components are taken from the Scientific Group Thermodata Europe database compiled by Dinsdale.[22] R_g is the gas constant. ${}^E G_m$ is the excess Gibbs free energy. $L_{i,j}$ and $L_{i,j,k}$ are, respectively, the binary and ternary interaction parameters between component i, j, and k. They are functions of temperature and alloy composition as given in Table I.

No experimental result on the interfacial energy between the Fe–Co-rich droplet and the matrix liquid can be found. We estimate σ as follows: generally, the interfacial energy between the two liquid phases coexisting during cooling an immiscible alloy in the miscibility gap satisfies[26]

$$\sigma = \sigma_0 \cdot (1 - T/T_C)^\delta \quad , \tag{12}$$

where T_C is the critical temperature of the immiscible system. σ_0 and δ are constants. Theoretically, δ takes a value 1.26 from the renormalization theory.[27] Calculations demonstrate that for the alloy of the composition Cu-10 wt% Co-10 wt% Fe, the critical temperature is about 1620 ± 10 K. The only parameter unknown is then σ_0. The numerical simulations demonstrate that the calculated average radius of the Fe–Co-rich particles has a favorable agreement with the experimental results when σ_0 equals 1.78 J/m^2. σ_0 is thus taken as 1.78 J/m^2.

The variation of the dynamic viscosity for liquid pure Cu, Co, Fe is calculated by Eq. (13). The dynamic viscosity for the Cu-rich matrix liquid is taken as the dynamic viscosity of pure Cu. The dynamic viscosity for the

https://doi.org/10.1557/jmr.2013.75 Published online by Cambridge University Press

TABLE I. Interaction parameters of the Cu–Co–Fe ternary system.

Phase	System	Parameters	Ref.
Liquid	Cu–Co	${}^{0}L^{\text{Liquid}}_{\text{Cu,Co}} = +34709.9 - 3.971T$	23
		${}^{1}L^{\text{Liquid}}_{\text{Cu,Co}} = -1164.9$	23
		${}^{2}L^{\text{Liquid}}_{\text{Cu,Co}} = +9639 - 4.651T$	23
	Cu–Fe	${}^{0}L^{\text{Liquid}}_{\text{Cu,Fe}} = +73316.72 - 142.79T + 15.82T \ln T$	24
		${}^{1}L^{\text{Liquid}}_{\text{Cu,Fe}} = +9100.15 - 5.94T$	24
		${}^{2}L^{\text{Liquid}}_{\text{Cu,Fe}} = +2428.96$	24
		${}^{3}L^{\text{Liquid}}_{\text{Cu,Fe}} = -233.62$	24
	Co–Fe	${}^{0}L^{\text{Liquid}}_{\text{Co,Fe}} = -9753.82$	25
		${}^{2}L^{\text{Liquid}}_{\text{Co,Fe}} = +505.82$	7
	Cu–Co–Fe	${}^{0}L^{\text{Liquid}}_{\text{Cu,Co,Fe}} = -32445 - 2.323T$	7
		${}^{1}L^{\text{Liquid}}_{\text{Cu,Co,Fe}} = +207886 - 120.246T$	7
		${}^{2}L^{\text{Liquid}}_{\text{Cu,Co,Fe}} = +1629 - 8.168T$	7

Fe–Co-rich droplets is taken as the mean dynamic viscosities of pure Fe and Co.

$$\eta = \eta_0 \exp(Q/R_g T) \quad , \tag{13}$$

where η_0 is constant. Q is the activation energy for viscous flow. They are given in Table II.[28]

The self-diffusion coefficient of Cu is calculated by using the Stokes–Einstein relation[29]:

$$D^{\text{Cu}} = \frac{k_B T}{6\pi\eta_m r_{\text{Cu}}} \quad . \tag{14}$$

The diffusivity of solute i in the liquid Cu is calculated by[30]

$$D^i = \frac{r_{\text{Cu}}}{r_i} D^{\text{Cu}} = \frac{k_B T}{6\pi\eta_m r_i} \quad , \tag{15}$$

where r_i is the ionic radius of element i. $r_{\text{Cu}} = 0.57$ Å, $r_{\text{Fe}} = 0.55$ Å, and $r_{\text{Co}} = 0.53$ Å.

D. Calculated results and discussions

The model was applied to calculate the microstructure formation in the gas atomized drops according to the practical experimental situations. The calculated 2D average radius of the Fe–Co-rich particles is shown in Fig. 4. It indicates that the 2D average radius of the Fe–Co-rich particles increases with the powder diameter according to $<R_{2D}> \propto d^{0.701}$. The favorable agreement between the experimental and the calculated results for the powders of different sizes indicates that the model describes the microstructure evolution process well.

Figure 6 shows the nucleation rate of the Fe–Co-rich droplets and the undercooling ($\Delta T_{L-L} = T_{\text{Binodal}} - T$, as shown in Fig. 5) for the liquid–liquid phase transformation as a function of temperature. When an initially homogeneous liquid is cooled into the metastable miscibility gap, it tends to decompose into two liquids. ΔT_{L-L} increases with the decrease of temperature and the liquid–liquid phase transformation begins when the undercooling of the matrix liquid reaches a critical value. Henceforth, the variation of the undercooling is a result of the concurrent actions of the drop of the melt temperature and the liquid–liquid phase transformation. The continuous cooling causes an increase in the undercooling while the nucleation and diffusional growth of the Fe–Co-rich droplets causes a decrease in the undercooling. In the early stage of the liquid–liquid phase transformation, both the nucleation rate and the number density of the Fe–Co-rich droplets are very low. The drop of the melt temperature dominates the variation of the undercooling. ΔT_{L-L} does not decrease but increases with the fall of temperature. The increase of the undercooling leads to a rapid rising in the nucleation rate and the number density of the Fe–Co-rich droplets. As a result, the rate at which the nucleation and growth of the Fe–Co-rich droplets consume Fe and Co increases, the composition of the matrix liquid begins to approach the equilibrium composition and the undercooling decreases quickly. Soon the nucleation ceases. A smaller atomized drop achieves a higher undercooling and, thus, an enhanced nucleation rate of the Fe–Co-rich

TABLE II. Viscosity parameters of liquid pure metal.

Metal	η_0 (mPa·s)	Q (KJ/mol)
Cu	0.3009	30.5
Co	0.255	44.4
Fe	0.3699	41.4

https://doi.org/10.1557/jmr.2013.75 Published online by Cambridge University Press

droplets and a wider temperature range for continuous nucleation.

The average radius and number density of the Fe–Co-rich droplets are shown in Fig. 7. The average radius of the Fe–Co-rich droplets changes slowly during the nucleation period because small Fe–Co-rich droplets are created continuously. After nucleation, the average radius of the Fe–Co-rich droplets increases rapidly because of the higher supersaturation of the matrix liquid. The growth of the droplets leads to a quick drop of the supersaturation and, thus, the growth rate of the droplets slows down gradually. The number density of the Fe–Co-rich droplets remains almost constant after nucleation, indicating that the effect of the spatial phase separation due to the Marangoni migration of the minority phase droplets is very weak, and also the Ostwald coarsening of the minority phase droplets is negligible under the rapid cooling conditions of gas atomization. Figure 8 shows the normalized radius distribution of the Fe–Co-rich droplets at different time during cooling a Cu–Co–Fe alloy in the miscibility gap for an atomized drop of 138 μm in diameter. It indicates that the sizes of the Fe–Co-rich droplets show a wider distribution during the nucleation period because the small nuclei are created continuously. The size distribution of the Fe–Co-rich droplets becomes narrower and develops into a symmetric shape quickly after the nucleation period since the growth rate increases with the decrease of the droplet size.

Calculations are carried out for the atomized drops of different diameters. It indicates that the average radius of the Fe–Co-rich particles decreases, whereas the number density of the Fe–Co-rich particles increases with the cooling rate of the atomized drop during the nucleation period of the Fe–Co-rich droplets ($\dot{T}_{\mathrm{Nuc}}$) as shown in Fig. 9. The average radius and number density of the Fe–Co-rich particles can, respectively, be related to $\dot{T}_{\mathrm{Nuc}}$ by $\langle R\rangle \propto \dot{T}_{\mathrm{Nuc}}^{-0.444}$ and $N \propto \dot{T}_{\mathrm{Nuc}}^{1.33}$.

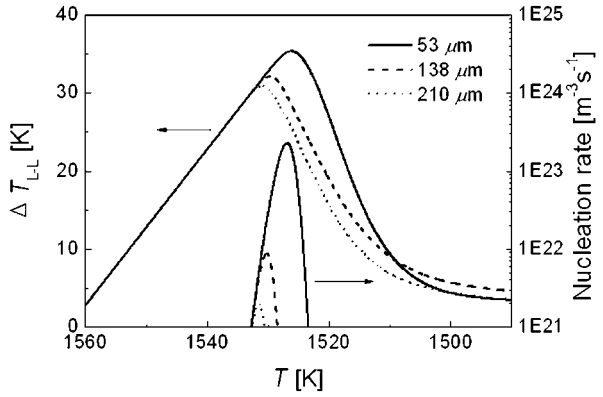


FIG. 6. Nucleation rate of the Fe–Co-rich droplets and undercooling of the matrix liquid during a cooling of the atomized drops of different diameters.

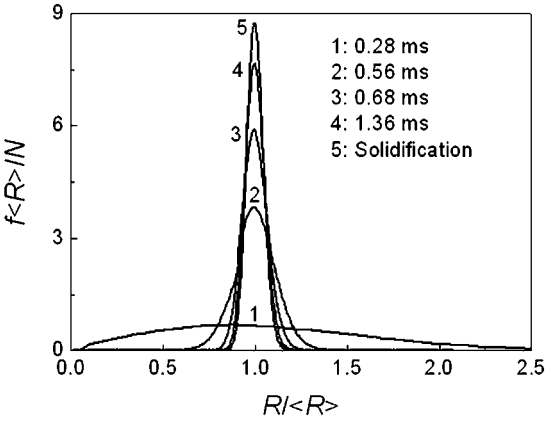


FIG. 8. Normalized distribution of the Fe–Co-rich droplets radii at the early (curve 1) and late stage (curve 2) of the nucleation and after the nucleation (curve 3–5) in an atomized drop of 138 μm in diameter.

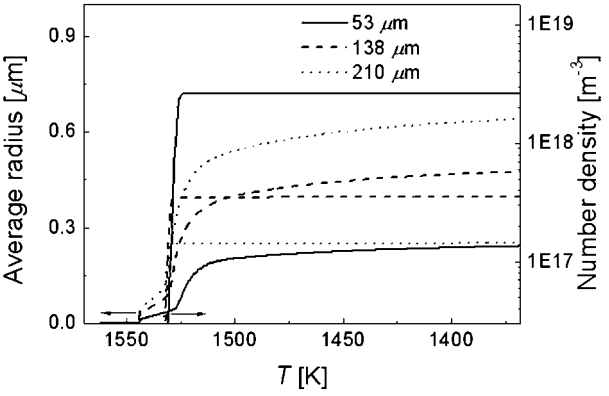


FIG. 7. Average radius and number density of the Fe–Co-rich droplets in the atomized drops of different diameters versus temperature.

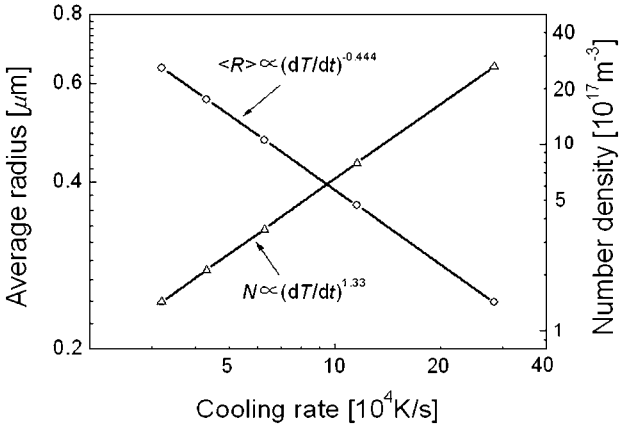


FIG. 9. Average radius and number density of the Fe–Co-rich particles as a function of the cooling rate of the atomized drop during the nucleation period of the Fe–Co-rich droplets.

https://doi.org/10.1557/jmr.2013.75 Published online by Cambridge University Press

IV. CONCLUSIONS

Ternary Cu-10 wt% Co-10 wt% Fe alloy was rapidly solidified by using the high-pressure gas atomization technique. The microstructure formation in a ternary Cu–Co–Fe alloy was analyzed. A model describing the microstructure evolution during the liquid–liquid phase transformation was developed. The microstructure formation in the gas atomized drops of Cu–Co–Fe alloy was simulated by coupling the thermodynamic and kinetic calculations. The numerical results showed a favorable agreement with the experimental results. The following conclusions are derived:

(1) The Cu-10 wt% Co-10 wt% Fe powders of the diameter <220 μm show a well-dispersed microstructure. The average radius of the Fe–Co-rich particles increases with the powder diameter.

(2) For Cu–Co–Fe alloy, under the rapid cooling conditions of gas atomization, the spatial phase separation due to the Marangoni migration of the minority phase droplets is very weak. Also the effect of Ostwald coarsening of the minority phase droplets on the microstructure evolution is negligible.

(3) For Cu-10 wt% Co-10 wt% Fe alloy, the average radius ($<R>$) and number density (N) of the Fe–Co-rich particles depend exponentially on the cooling rate of the melt during the nucleation period of the Fe–Co-rich droplets ($\dot{T}_{\mathrm{Nuc}}$) according to $\langle R\rangle \propto \dot{T}_{\mathrm{Nuc}}^{-0.444}$ and $N \propto \dot{T}_{\mathrm{Nuc}}^{1.33}$.

ACKNOWLEDGMENTS

This work is financially supported by the National Natural Science Foundation of China (Grant Nos. 51031003, 51071159, and 51271185).

REFERENCES

1. C. Biselli and D.G. Morris: Microstructure and strength of Cu-Fe in situ composites after very high drawing strains. *Acta Mater.* **44**, 493–504 (1996).
2. A.E. Berkowitz, J.R. Mitchell, M.J. Carey, A.P. Young, S. Zhang, F.E. Spada, F.T. Parker, A. Hutten, and G. Thomas: Giant magnetoresistance in heterogeneous Cu-Co alloys. *Phys. Rev. Lett.* **68**, 3745–3748 (1992).
3. A. Munitz, S.P. Elder-Randall, and R. Abbaschian: Supercooling effects in Cu-10 Wt Pct Co alloys solidified at different cooling rates. *Metall. Mater. Trans. A* **23A**, 1817–1827 (1992).
4. Y. Nakagawa: Liquid immiscibility in copper-iron and copper-cobalt systems in the supercooled state. *Acta Metall.* **6**, 704–711 (1958).
5. C.D. Cao, D.M. Herlach, M. Kolbe, G.P. Görler, and B. Wei: Rapid solidification of $Cu_{84}Co_{16}$ alloy undercooled into the metastable miscibility gap under different conditions. *Scr. Mater.* **48**, 5–9 (2003).
6. J.J. Guo, Y. Liu, J. Jia, Y.Q. Su, and H.S. Ding: Coarsening process of minority phase droplets during rapidly cooling an immiscible alloy through the miscibility gap. *Acta. Metall. Sin.* **37**, 363–368 (2001).
7. M.A. Turchanin, L.A. Dreval, A.R. Abdulov, and P.G. Agraval: Mixing enthalpies of liquid alloys and thermodynamic assessment of the Cu-Fe-Co system. *Powder Metall. Met. Ceram.* **50**, 98–116 (2011).
8. D.I. Kim and R. Abbaschian: The metastable liquid miscibility gap in Cu-Co-Fe alloys. *J. Phase Equilib.* **21**, 25–31 (2000).
9. A. Munitz, A.M. Bamberger, S. Wannaparhun, and R. Abbaschian: Effects of supercooling and cooling rate on the microstructure of Cu-Co-Fe alloys. *J. Mater. Sci.* **41**, 2749–2759 (2006).
10. S. Curiotto, L. Battezzati, E. Johnson, M. Palumbo, and N. Pryds: The liquid metastable miscibility gap in the Cu-Co-Fe system. *J. Mater. Sci.* **43**, 3253–3258 (2008).
11. M. Bamberger, A. Munitz, L. Kaufman, and R. Abbaschian: Evaluation of the stable and metastable Cu-Co-Fe phase diagrams. *Calphad* **26**, 375–384 (2002).
12. C.P. Wang, X.J. Liu, I. Ohnuma, R. Kainuma, and K. Ishida: Phase equilibria in Fe-Cu-X (X: Co, Cr, Si, V) ternary systems. *J. Phase. Equilib.* **23**, 236–245 (2002).
13. M. Palumbo, S. Curiotto, and L. Battezzati: Thermodynamic analysis of the stable and metastable Co-Cu and Co-Cu-Fe phase diagrams. *Calphad* **30**, 171–178 (2006).
14. F.P. Dai, C.D. Cao, and B.B. Wei: Phase separation and rapid solidification of liquid $Cu_{60}Fe_{30}Co_{10}$ ternary peritectic alloy. *Sci. China, Ser. G* **50**, 509–518 (2007).
15. L. Granasy and L. Ratke: Homogeneous nucleation within the liquid miscibility gap of Zn-Pb alloys. *Scr. Mater.* **28**, 1329–1334 (1993).
16. J.Z. Zhao, L. Ratke, and B. Feuerbacher: Microstructure evolution of immiscible alloys during cooling through the miscibility gap. *Modell. Simul. Mater. Sci. Eng.* **6**, 123–139 (1998).
17. J.A. Marqusee and J. Ross: Theory of Ostwald ripening: Competitive growth and its dependence on volume fraction. *J. Chem. Phys.* **80**, 536–543 (1984).
18. J.Z. Zhao: The kinetics of the liquid-liquid decomposition under the rapid solidification conditions of gas atomization. *Mater. Sci. Eng., A* **454–455**, 637–640 (2007).
19. W.E. Ranz and W.R. Marshall: Evaporation from drops. *Chem. Eng. Prog.* **48**, 141–146 (1952).
20. P.S. Grant, B. Cantor, and L. Katgerman: Modelling of droplet dynamic and thermal histories during spray forming I. Individual droplet behavior. *Acta Metall. Mater.* **41**, 3097–3108 (1993).
21. S.V. Patankar: *Numerical Heat Transfer and Fluid Flow* (McGraw-Hill, New York, 1980).
22. A.T. Dinsdale: SGTE data for pure elements. *Calphad* **15**, 317–425 (1991).
23. M.A. Turchanin and P.G. Agraval: Phase equilibria and thermodynamics of binary copper systems with 3d-metals. V. Copper–cobalt system. *Powder Metall. Met. Ceram.* **46**, 77–89 (2007).
24. M.A. Turchanin, P.G. Agraval, and I.V. Nikolaenko: Thermodynamics of alloys and phase equilibria in the copper–iron system. *J. Phase Equilib.* **24**, 307–319 (2003).
25. I. Ohnuma, H. Enoki, O. Ikeda, R. Kainuma, H. Ohtani, B. Sundman, and K. Ishida: Phase equilibria in the Fe–Co binary system. *Acta Mater.* **50**, 379–393 (2002).
26. G. Kaptay: On the temperature gradient induced interfacial gradient force, acting on precipitated liquid droplets in monotectic liquid alloys. *Mater. Sci. Forum* **508**, 269–274 (2006).
27. M.R. Moldover: Interfacial tension of fluids near critical points and two-scale-factor universality. *Phys. Rev. A* **31**, 1022–1033 (1985).
28. E.A. Brandes and G.B. Brook (eds.): *Smithells Metals Reference Book*, 7th ed. (Butterworth-Heinemann, Oxford, 1992).
29. A.I. Pommrich, A. Meyer, D. Holland-Moritz, and T. Unruh: Nickel self-diffusion in silicon-rich Si-Ni melts. *Appl. Phys. Lett.* **92**, 241922 (2008).
30. A.K. Roy and R.P. Chhabra: Prediction of solute diffusion coefficients in liquid metals. *Metall. Trans. A* **19A**, 273–279 (1988).

https://doi.org/10.1557/jmr.2013.75 Published online by Cambridge University Press